Zebrafish airinemes optimize their shape between ballistic and diffusive search

Sohyeon Park[1†], Hyunjoong Kim[2†], Yi Wang[3], Dae Seok Eom[1,3]*, Jun Allard[1,4,5]*

[1]Center for Complex Biological Systems, University of California, Irvine, Irvine, United States; [2]Center for Mathematical Biology, Department of Mathematics, University of Pennsylvania, Philadelphia, United States; [3]Department of Developmental & Cell Biology, University of California, Irvine, Irvine, United States; [4]Department of Physics and Astronomy, University of California, Irvine, Irvine, United States; [5]Department of Mathematics, University of California, Irvine, Irvine, United States

Abstract In addition to diffusive signals, cells in tissue also communicate via long, thin cellular protrusions, such as airinemes in zebrafish. Before establishing communication, cellular protrusions must find their target cell. Here, we demonstrate that the shapes of airinemes in zebrafish are consistent with a finite persistent random walk model. The probability of contacting the target cell is maximized for a balance between ballistic search (straight) and diffusive search (highly curved, random). We find that the curvature of airinemes in zebrafish, extracted from live-cell microscopy, is approximately the same value as the optimum in the simple persistent random walk model. We also explore the ability of the target cell to infer direction of the airineme's source, finding that there is a theoretical trade-off between search optimality and directional information. This provides a framework to characterize the shape, and performance objectives, of non-canonical cellular protrusions in general.

*For correspondence:
dseom@uci.edu (DSeokE);
jun.allard@uci.edu (JA)

[†]These authors contributed equally to this work

Editor's evaluation

This article studies statistical aspects of the role of long-range cellular protrusions called airinemes as means of intracellular communication. The authors use published data showing how airinemes approach a target cell and describe these movements with a mathematical model for an unobstructed persistent random walk. Beyond the specialized readers interested in modeling and airineme biology, this article will also be of interest to cell biologists and biophysicists interested in intracellular communication.

Introduction

The question of optimal search — given a spatiotemporal process, what parameters allow a searcher to find its target with greatest success? — arises in many biological contexts for a variety of spatiotemporal processes. Examples of relevant processes include searchers moving by diffusion or random walks (*Lawley et al., 2020*; *Berg and Purcell, 1977*), Levy walks (*Fricke et al., 2016*), and ballistic motion (straight trajectories [*Bressloff, 2020*], which, e.g., arises in chromosome search by microtubules [*Holy et al., 1994*; *Paul et al., 2009*]), and combinations of these (*Berg, 1993*). Another type of motion is the persistent random walk (PRW), which has intermediate properties between diffusion and ballistic motion. PRWs have been studied in continuous space (*Schakenraad et al., 2020*; *Großmann et al., 2016*; *Khatami et al., 2016*) and on a lattice (*Tejedor et al., 2012*), have been used with variants to model cell migration (*Jones et al., 2015*; *Weavers et al., 2016*; *Harrison and Baker, 2018*), and are mathematically equivalent to worm-like chains, which have been used to study the search by
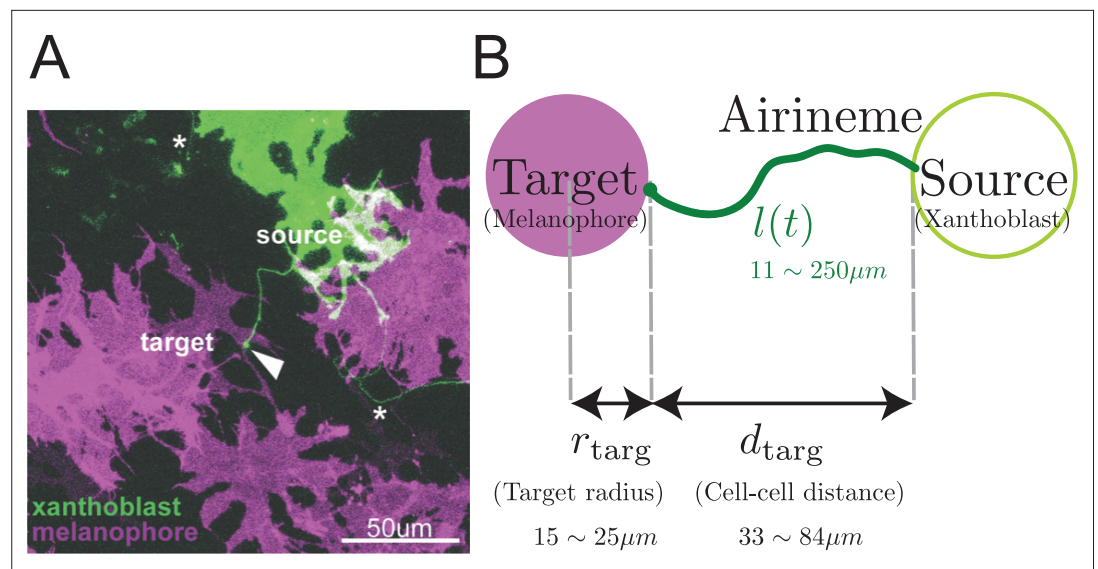
Figure 1. Airineme-mediated signaling between xanthoblast and target melanophore. (**A**) Multiple airinemes extend from xanthoblast (undifferentiated yellow pigment cell, green). Airineme makes successful contact (arrowhead) with melanophore cell (pigment cell, purple). Asterisks indicate airinemes from other sources. Scale bar: 50 μm. (**B**) Model schematic. A single airineme extends from the source (right, green circle) and searches for the target cell (left, purple circle). Target cell has radius r_{targ} and has distance d_{targ} away from the origin. The airineme's contour length at time t is $l(t)$.

a polymer for a binding partner (*Mogre et al., 2020*). For all the above processes, optimality depends on parameters of the searcher (e.g., whether searchers operate individually or many in parallel; *Schuss et al., 2019*; *Lawley and Madrid, 2020*), the target(s), and the environment (*De Bruyne et al., 2020*; *Bressloff, 2020*).

One example of a biological search process arises during organismal development, when cells must establish long-range communication. Some of this communication occurs by diffusing molecules (*Hu et al., 2010*; *Govern and ten Wolde, 2012*; *Bialek and Setayeshgar, 2008*; *Endres and Wingreen, 2009*) like morphogens. However, recently, an alternative cell–cell communication mechanism has been revealed to be long, thin cellular protrusions extending tens to hundreds of micrometers (*Eom, 2020*; *Yamashita et al., 2018*; *Caviglia and Ober, 2018*; *Sanders et al., 2013*; *Bressloff and Kim, 2019*; *Inaba et al., 2015*). These include cytonemes (*Kornberg and Roy, 2014*), tunneling nanotubes (*Zurzolo, 2021*), tenocyte projections (*Subramanian et al., 2018*), and airinemes in zebrafish (*Volkening and Sandstede, 2018*; *Volkening, 2020*; *Eom and Parichy, 2017*; *Eom et al., 2015*), shown in *Figure 1A*. One of the difficulties delaying their discovery and characterization is their thin, suboptical width, and the fact that they only form at specific stages of development (*Eom, 2020*; *Yamashita et al., 2018*; *Caviglia and Ober, 2018*).

Airinemes are produced by xanthoblasts (undifferentiated yellow pigment cells) and play a role in the spatial organization of pigment cells that produce the patterns on zebrafish skin (*Eom et al., 2015*; *Eom and Parichy, 2017*; *Eom, 2020*; *Volkening and Sandstede, 2018*). Macrophages recognize a signal on xanthoblasts and begin dragging a protruding airineme from the xanthoblast as they migrate around the tissue, with the airineme trailing behind them. Airineme lengths have a maximum, regardless of whether they reach their target. If the tip complex reaches a target before this length, it recognizes target cells (melanophores) and the macrophage and airineme tip disconnect. The airineme tip contains the Delta-C ligand, which activates Notch signaling in the target cell. Due to experimental limitations on spatial and temporal resolution, the mechanism by which the airineme tip complex (which might include the entire macrophage) recognizes the target is still mysterious, as is the mechanism by which the macrophage hands off the airineme tip. It is also not known what other signals, if any, are carried by the airineme. If no target cell is found by the maximum length, the macrophage and airineme disconnect, and the airineme retracts. In the unrelated context of wound-healing, macrophages are recruited to the site of injury by detecting chemokines released by damaged cells
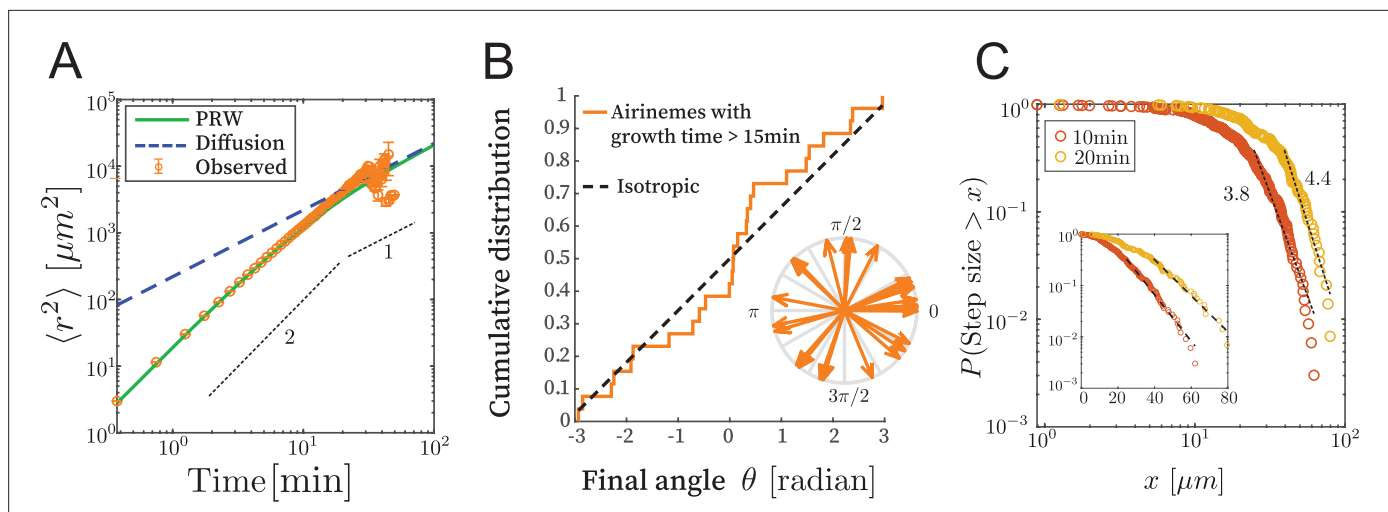
Figure 2. Airinemes are not consistent with simple random walk or Levy-type models. (**A**) Mean squared displacement (MSD) of airinemes. Airineme experimental MSDs have exponent ≈ 2 (corresponding to slope in log–log plot) up to ≈ 15 min, arguing against a simple random walk model. $N = 70$ airinemes. (**B**) For airinemes with growth periods longer than 15 min, the distribution of final angles, that is, the angle between the tangent vector at the airineme's origin and the tangent vector at its tip. This is consistent with isotropy, that is, a uniform distribution in $(-\pi, \pi)$, shown as a dashed line (Kolmogorov–Smirnov test, $N = 26$, p-value 0.37). The results of this test are insensitive to the cutoff length (see *Figure 2—source data 1*). (**C**) Step length complementary cumulative distribution function (CCDF). Levy models in 2D are characterized by CCDF tails with an exponent between 1 and 3. However, for two different time sampling intervals (10 and 20 min, from $N = 56$ airinemes), the tails of the distribution fit to an exponent greater than 3, and a continued downward curvature instead of a power-law, arguing against Levy models. Inset shows same data, same time sampling intervals, and same axes, but on semi-log plot.

The online version of this article includes the following source data and figure supplement(s) for figure 2:

Source data 1. Final angles are isotropic.

Figure supplement 1. Time evolution and final state are self-consistent.

or other immune cells. In contrast, macrophages pulling airinemes during development are not triggered by tissue damage or infections in zebrafish skin (*Eom et al., 2015*), and there is no experimental evidence that the airineme search process responds to any directional cues.

For diffusing cell–cell signals, dynamics are characterized by a diffusion coefficient. In contrast, cellular protrusions require more parameters to describe, for example, a velocity and angular diffusion, or equivalently a curvature persistence length. Here, we ask, what are these parameters, and what determines their values? We focus on airinemes where quantitative details have been measured (*Eom and Parichy, 2017*; *Eom et al., 2015*). We find that airineme shape is most consistent with a finite-length PRW model, and that the parameters of this model exhibit an optimum for minimizing the probability of finding a target (or, equivalently, the mean number of attempts). We compare this with another performance objective, the ability for the airineme to provide a directional cue to the target cell, and find that there is a theoretical trade-off between these two objectives. This work provides an example where a readily observable optimum appears to be obtained by a biological system.

Results
Airinemes are consistent with a finite PRW model

We examined time-lapse live-cell image data as described in *Eom and Parichy, 2017* and *Eom et al., 2015*. We confirmed that the time series and the final state are similar (*Figure 2—figure supplement 1*), meaning that the shape of the part of the airineme existing at time t does not significantly change after time t, as the tip of the airineme continues to extend. This allows us to consider only the fully extended airineme and infer the dynamics, assuming airinemes extend with constant velocity v = 4.5 μm/min (*Eom et al., 2015*). This removes artifacts like microscope stage drift and drastically simplifies the analysis. We manually identified and discretized 70 airinemes into 5596 position vectors $r(t)$, and from these, computed the mean squared displacement (MSD) $\langle r^2 \rangle$. Random walks satisfy $\langle r^2 \rangle = 4Dt$.

However, the observed MSD, shown in *Figure 2A*, does not appear linear in t. We fit it to $\langle r^2 \rangle = \gamma t^\alpha$ and found the best-fit exponent α of 1.55 (90% CI in [1.50,1.61]), and indeed it appears that a single exponent is not appropriate across orders of magnitude. We therefore reject the simple random walk description.

Next, we consider Levy-type models such as those that have been used to describe animal optimal foraging (*Viswanathan et al., 2011*) and T cell migration (*Fricke et al., 2016*). These processes have a step size distribution whose tail has exponent between 1 and 3 in 2D (*Fricke et al., 2016*; *Viswanathan et al., 2011*), where step size is the displacement during a specified time interval. We revisit the time-series data (i.e., here we do not use the final state approximation) and compute a step length complementary cumulative distribution function (CCDF). For two time interval choices, shown in *Figure 2B*, the best-fit CCDF exponents are greater than 3 (for 10 min, exponent is 3.81 with 90% CI in [3.68,3.95]; for 20 min, exponent is 4.40 with 90% CI in [4.18,4.61]). Indeed, the CCDFs at two different time sampling intervals have continued downward curvature, indicating that a power-law description is inappropriate. We thus conclude that the process is not consistent with Levy-type models.

Finally, we consider a finite-length PRW. In this model, the tip of the airineme moves at constant speed v, while the direction undergoes random changes with parameter D_θ, the angular diffusion coefficient. This parameter has units inverse minutes and roughly corresponds to the 'curviness' of the path. The dynamics are governed by *Equations 2–4*. A key observation from time-lapse imaging is that airinemes have a maximum length, after which the search process terminates if unsuccessful. Thus, our PRW model is finite-length, meaning that we assume the airinemes extend only up to $l_{max} = 250\,\mu m$. This assumption yields a final length distribution (*Figure 3*, *Figure 3—figure supplement 1*) consistent with the observed distribution (*Eom et al., 2015*).

The airineme MSD fits the prediction of the PRW model, in *Equation 5*, up to time point around 15 min. Above this time, the PRW model is consistent with the data, although the low number of long airinemes in our data precludes a strong conclusion from MSD alone. We therefore took all airinemes whose growth time was greater than 15 min and plotted their final angle, that is, the angle between the tangent vector at their point of emergence from the source cell and the tangent vector at their tip. The PRW model predicts that, for long times $> 1/D_\theta$, the angular distribution should become isotropic. In *Figure 2B*, we find that the angular distribution is uniform, that is, isotropic (Kolmogorov–Smirnov test p-value 0.37, $N = 26$). Since there are relatively few data points, we repeated this analysis under various airineme selection criteria, which includes up to $N = 49$ airinemes, and in all cases found the final angular distribution to be consistent with uniformity (*Figure 2—source data 1*). (In *Figure 4*, we also check the autocorrelation function and further confirm consistency with the PRW model.) Taken together, the data favor the PRW model, which we use in the following analysis.

We also assume that airinemes operate independently as there is no evidence of airinemes communicating with each other during the search process. Furthermore, airinemes are generated at approximately 0.15 airinemes per cell per hour. Thus, the mean time between airineme initiations is $\approx 400\,min$, much larger than the time each airineme extends, which is 56 min. Note that many airinemes emanating from the same source cell may exist simultaneously, but most of the time only one airinemes is extending. Also, while the tissue surface is crowded, the airineme tips (which are transported by macrophages; *Eom et al., 2015*) appear unrestricted in their motion on the 2D surface, passing over or under other cells unimpeded (*Eom and Parichy, 2017*). We therefore do not consider obstacles in our model (although these have been studied in other PRW contexts; *Schakenraad et al., 2020*; *Khatami et al., 2016*; *Hassan et al., 2019*). This includes the source cell, that is, we allow the search process to overlie the source cell.

The target cell is modeled as a circle of radius $r_{targ} = 15 - 25\,\mu m$ (*Eom et al., 2015*), separated from the source of the airineme by a distance $d_{targ} \approx 50\,\mu m$, as shown in *Figure 1B*. Including the position and size of the target, the model has five parameters, all of which have been measured (see *Table 1* and *Eom et al., 2015*; *Ryu et al., 2016*) except for D_θ.

Contact probability is maximized for a balance between ballistic and diffusive search

We performed simulations of the PRW model, testing different angular diffusion values for different values of cell-to-cell distance and target cell radius. For each parameter set, we measured the proportion of simulations that contacted the target. Specifically, contact is defined as the event in which the
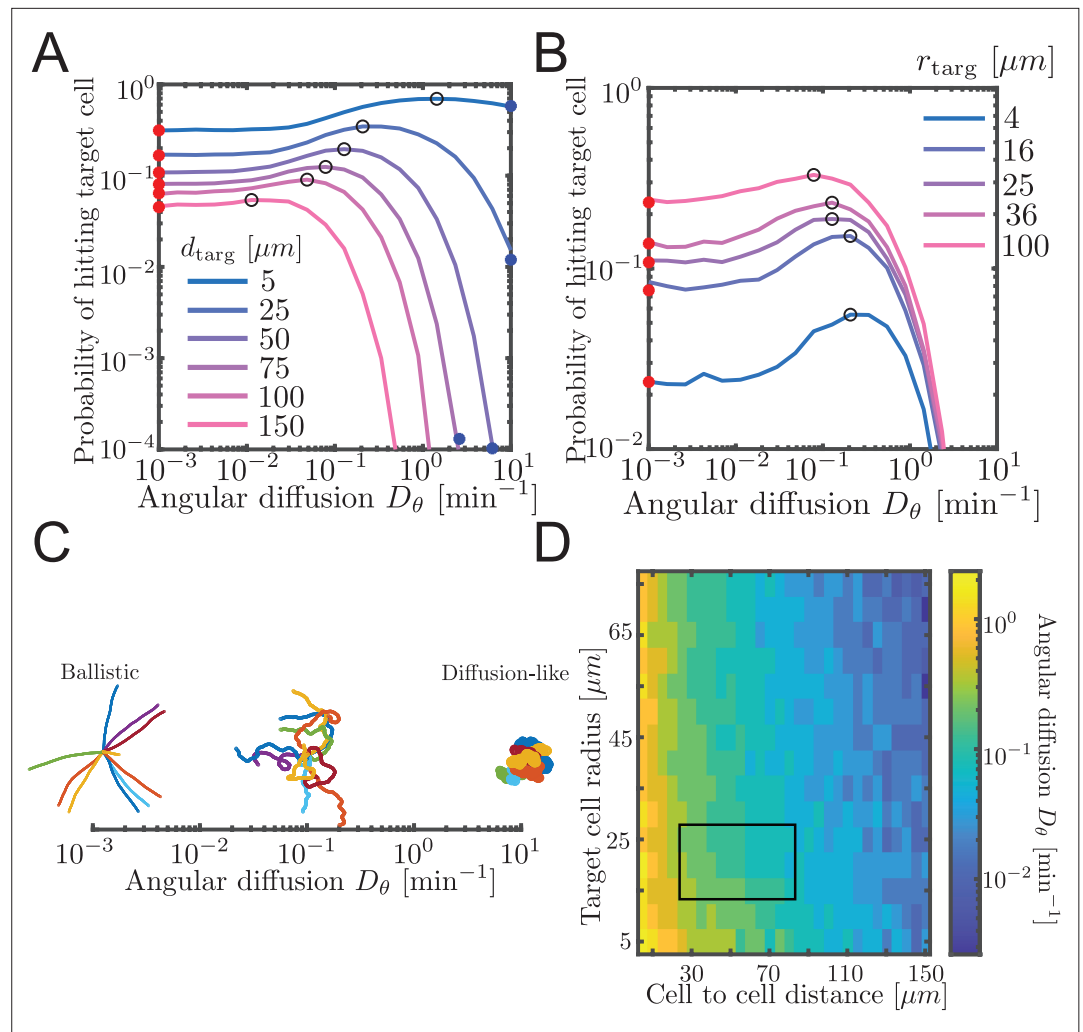
Figure 3. Probability to contact a target cell is maximized by a balance between ballistic search and diffusion-like search. (**A, B**) Simulated airineme target search for various D_θ. The values of D_θ that leads to the highest search success probability are shown as black open circles. Theoretical values for ballistic limit from Equation 6 are shown as red circles. (**A**) Varying distances between the target and the source cell, while fixing the target cell radius at 25 µm. We validate simulation results with survival probability PDE at high D_θ from **Equation 7**, shown in blue circles. (**B**) Varying target cell radii while fixing the distance between the target and the source. For the biologically relevant parameter ($d_{\text{targ}} \sim 50\,\mu$m), optimal angular diffusion is around $D_\theta \sim 0.18\,\text{min}^{-1}$. (**C**) Qualitative behavior of airineme target search depends on D_θ. (**D**) Optimal D_θ for a larger range of cell-to-cell distances and target cell radii. Rectangular region shows biologically relevant parameters.

The online version of this article includes the following figure supplement(s) for figure 3:

Figure supplement 1. Final lengths of airinemes.

Figure supplement 2. Simulated contact success shown as number of attempts instead of probability of contact.

---

tip of the growing airineme intersects with the target. In simulations, we assume contact has occurred when the airineme tip reaches within a distance r_{targ} of the center of the target cell. We refer to r_{targ} as the target cell radius. However, as discussed above, the mechanism by which contact is detected is unknown, and it could be that the airineme tip has a large effective spatial extent that includes some or all of the macrophage. Note again the search process is finite-length (otherwise in two dimensions would always eventually find the target). These contact probabilities are shown in **Figure 3A and B**. Equivalently, we plot the inverse, the mean number of attempts, in **Figure 3—figure supplement 2**.

We find that there exists an optimal angular diffusion coefficient that maximizes the chance to contact the target cell. The optimal value balances between ballistic and diffusion-like search. This has
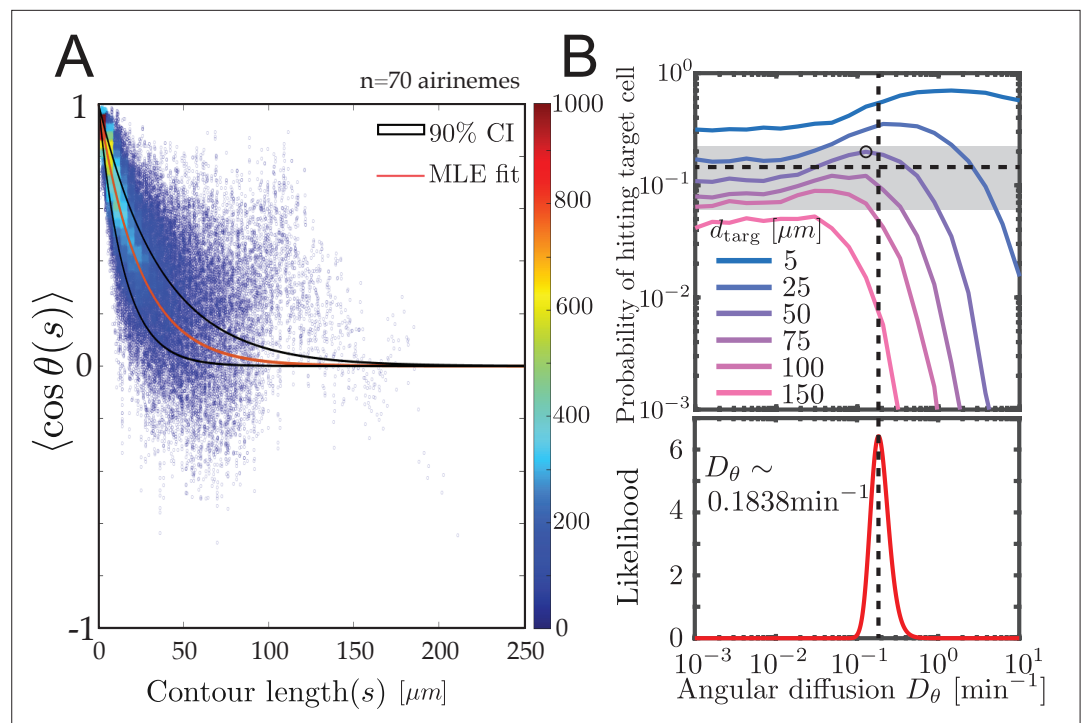
Figure 4. Experimental airineme curvature agrees with the optimal curvature. (**A**) Orientation autocorrelation function. We measure tangent angles $\cos(\theta)$ at 5596 points along 70 airinemes, and then compute the likelihood function (**B**, bottom) of D_θ fit to **Equation 1**. Best-fit curve is shown as red with a 90% confidence interval shown in black. Blue dots and heatmap were generated using a moving average with a window of 10 nearest data points and the heatscatter MATLAB function. (**B**) Bottom: we find that the best-fit airineme curvature from maximum likelihood estimation is $D_\theta = 0.1838\text{min}^{-1}$. We find that this value is similar to the D_θ that optimizes contact probability for the biologically relevant target cell distance $d_\text{targ} = 50\,\mu\text{m}$ (top). The experimentally observed probability of contact per airineme, center estimate (horizontal dashed line), and 90% confidence interval (gray area) are also shown.

The online version of this article includes the following figure supplement(s) for figure 4:

Figure supplement 1. Experimental data analysis method validation and data collection.

been previously shown for infinite, on-lattice PRWs (**Tejedor et al., 2012**) and worm-like chain models searching for binding partners (**Mogre et al., 2020**). We heuristically understand it as follows. When D_θ is small (**Figure 3C**, left), airinemes are straight and therefore move outward a large distance, which is favorable for finding distant targets. However, straight airinemes easily miss targets. On the other hand, for D_θ large (**Figure 3C**, right), the airineme executes a random walk. Random walks are locally thorough, so do not miss nearby targets, but the search rarely travels far. Thus, if the target cell is small or close, a diffusion-like search process is favored, but if the target cell is far or large, then a ballistic

Table 1. Parameter values.

Symbol	Meaning	Estimate and value used	Source
l_{max}	Maximum length of airineme	250 µm	*Figure 3—figure supplement 1*
v	Velocity of airineme growth	4.5 µm (1.4–12 µm, N = 929)	*Eom et al., 2015*
d_{targ}	Distance to target cell	51 µm (33–84 µm, N = 70)	*Eom et al., 2015*
r_{targ}	Target cell radius	15–25 µm	*Ryu et al., 2016*
D_θ	Angular diffusion	$0.1838\,\text{rad}^2/\text{min}$	Estimated here

search is favored. We confirm this in *Figure 3D*, where we plot optimal D_θ over a large range of target cell radii and cell-to-cell distances. For the biologically relevant parameters (rectangular region in *Figure 3D*), a balance between ballistic and diffusion-like is optimal.

Experimental airineme curvature is approximately optimal

In order to estimate the missing parameter D_θ, we use the angular autocorrelation function

$$\langle \cos \theta(s) \rangle = \exp\left(-D_\theta s/v\right) \tag{1}$$

shown in *Figure 4*. We performed manual image analysis and maximum likelihood estimation to fit *Equation 1*, along with model convolution (*Figure 4—figure supplement 1*, *Gardner et al., 2010*, Materials and methods) to estimate uncertainty.

We find the maximum likelihood estimated persistence length of $12.24\,\mu$m, corresponding to an angular diffusion $D_\theta = 0.184\,\text{min}^{-1}$. Surprisingly, as shown in *Figure 4B*, this value matches our simulated optimal angular diffusion value for the biologically relevant parameter values. Moreover, in the experimental data, we find that the proportion making successful contact with target cells is $P_{\text{contact}} = 0.15$ (horizontal dashed line), from $N = 49$ airinemes with a 90% confidence interval in $[0.06, 0.24]$ (gray box in *Figure 4B*). This also agrees surprisingly well with the model prediction $p_{\text{contact}} \approx 0.185$.

Directional information at the target cell

In some models of zebrafish pattern formation, the target cells receive directional information from source cells (*Eom, 2020*; *Volkening, 2020*), that is, the target cell must determine where the source cell is, relative to the target's current position. We explore the hypothesis that airineme contact itself could provide directional information since the location on the target cell at which the airineme contacts, θ_{contact} as shown in *Figure 5A*, is correlated with the direction of the source cell. Analogous directional sensing is possible by diffusive signals, where physical limits have been computed in a variety of situations (*Lawley et al., 2020*; *Berg and Purcell, 1977*).

We examined the contact angle distribution on the target cell. In *Figure 5B*, we show this distribution for three values of D_θ: low (ballistic), high (diffusion-like), and the observed value we found above. The source cell is placed at $\theta_{\text{origin}} = 0$ without loss of generality (its initial direction is still chosen uniformly randomly). We show the distribution of contact angles on the target cell $p(\theta_{\text{contact}}|\theta_{\text{origin}} = 0)$ as both a radial histogram (top) and cumulative distribution (bottom). Interestingly, we find that the observed airineme parameters lead to a wide distribution of contact angles compared to both ballistic or diffusion-like airinemes.

To quantify the ability of the target cell to sense the direction of the source by arrival angle of a single airineme, we use Fisher information (*Fisher, 1997*), modified to take into account the probabilistic number of airinemes that a target cell receives, using *Equation 9*. Using this measure, we observe a minimum at intermediate D_θ, shown in *Figure 5C*. We understand this intuitively as follows. For very straight airinemes, the allowed contact locations are restricted to a narrow range (a straight airineme can never hit the target's far side), resulting in high directional information. For high D_θ, we initially expected low and decreasing directional information since there is more randomness. However, these are finite-length searches, and the spatial extent of the search process shrinks as D_θ increases. This leads to a situation where the tip barely reaches the target, and only at closest points (near $\theta_{\text{contact}} = 0$), resulting again in high directional information.

To compare with experimental observations, we attempted to measure the contact angle distribution of airinemes in contact with target cells. This is complicated by the highly noncircular shape of these cells, so we approximate the angle by connecting three points: the point on the source cell from which the airineme begins, the center of the nucleus of the target, and the point on the surface of the target where the airineme makes contact, as shown in *Figure 5—figure supplement 1*. We find a modified Fisher information of 5.7×10^{-5}, slightly smaller but similar in magnitude to the angle distribution predicted by the simulation.

Trade-off between directional sensing and contact probability

By inspecting both P_{contact} and directional information shown in *Figure 5D*, we find that there is a trade-off between the searcher's contact success and the target cell's directional sensing. Heuristically,
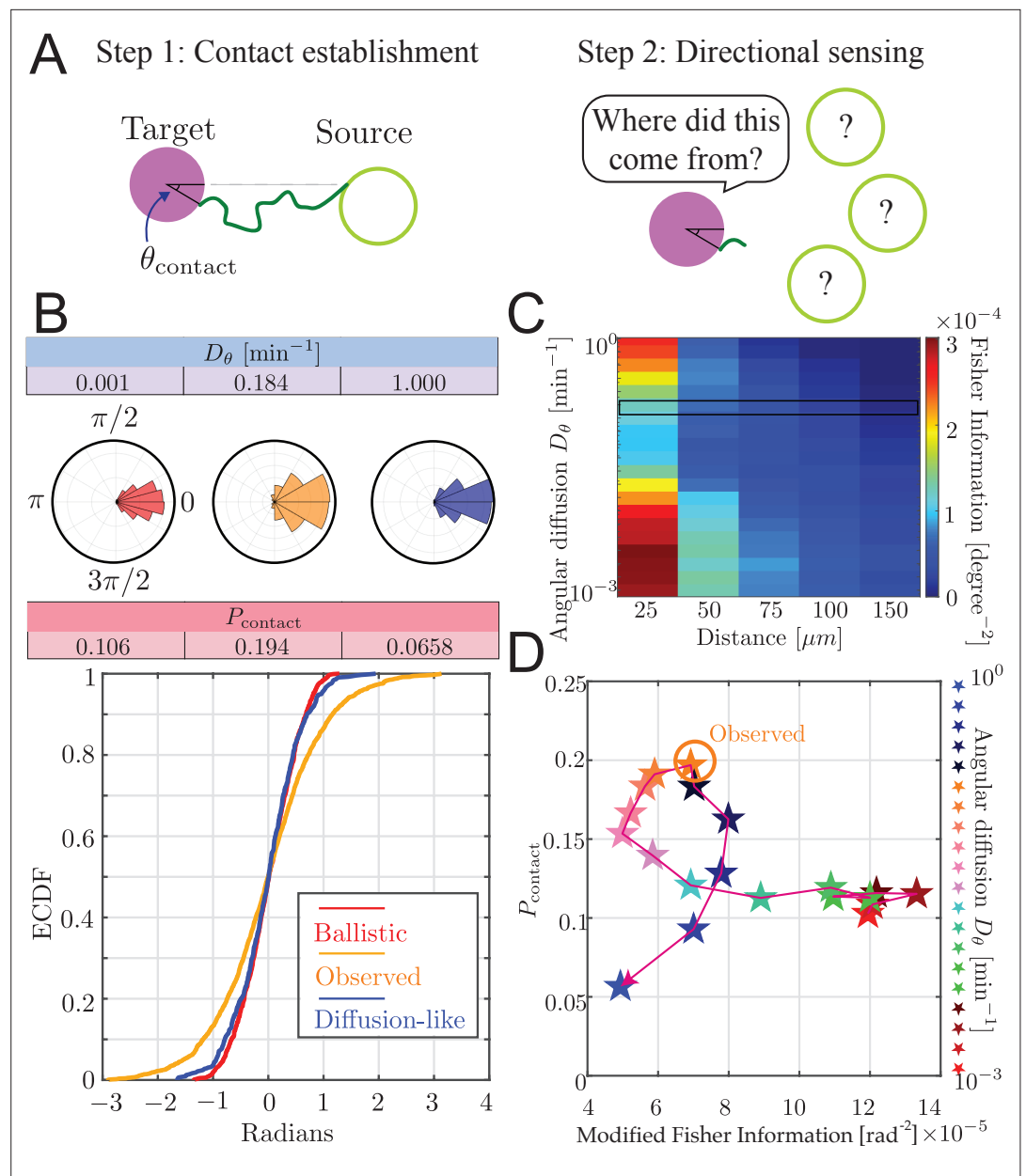
Figure 5. Trade-off between airineme directional sensing information and the probability of contacting the target cell. (**A**) Given that the source cell is located at $\theta = 0$, the distribution of angles at which the airineme contacts the target cell. (**B**) Given a source cell is located at $\theta = 0$, the distribution of angles at which the airineme contacts the target cell. Angle distributions with higher variance indicate poorer directional sensing. Three angular diffusion values (near ballistic limit, experimentally observed, and near diffusion limit) are shown. (**C**) Directional sensing accuracy, quantified using the modified Fisher information (FI) *Equation 9*, for different source-to-target distances and different ranges of angular diffusion values are tested, while fixing target cell radius at 25 μm. Black rectangular region shows the FI values for the observed airineme curvature. (**D**) Relationship between the contact probability $P_{contact}$ and FI for a range of D_θ (increasing with direction of arrow).

The online version of this article includes the following figure supplement(s) for figure 5:

Figure supplement 1. Experimental measurement of contact angle and directional information.

Figure supplement 2. Trade-off between directional sensing and contact probability for range of parameters.

this is because the two objectives prefer opposite variances. To maximize contact probability, variance should be maximal, taking full advantage of the surface of the target. On the other hand, to maximize directional information, the variance of contact angle should be minimized.

Interestingly, the experimentally observed D_θ is at a point where either increasing or decreasing its value would suffer one or the other objectives, a property known as Pareto optimality (**Alon, 2009**; **Barton and Sontag, 2013**). Note that this is also the D_θ value that maximizes search success, so the data is consistent with either conclusion that the curvature is optimized for search or it is optimized to balance search and directional information. In other words, in the case of zebrafish airinemes, there is no evidence that the shape of these protrusions sacrifices the goal of optimal search in order to achieve increased directional signaling. We wondered whether this is a general feature of search by PRW. The parametric curve in **Figure 5D** has a peculiar loop, the concave-down region giving rise to the Pareto optimum. In **Figure 5—figure supplement 2**, we show the parametric curve for a range of distances to the target d_{targ} and target sizes r_{targ}. Note that we do not explicitly explore l_{max}, but since these plots have not been nondimensionalized, the parametric curve for a different l_{max} can be obtained by rescaling the results shown. At low d_{targ} (top row of **Figure 5—figure supplement 2**), the trade-off is amplified, and the parametric curve resembles bull's horns with two tips representing the smallest and largest D_θ in our explored range, pointing outward so the shape is concave-up. Intuitively, we understand this as follows: since the target is fairly close (relative to l_{max}), contact is easy. But the only way to get directional specification is by increasing D_θ to be very large, effectively shrinking the search range so it only reaches (with significant probability) the target at the near side at $\theta_{\text{contact}} = 0$. The parametric curve is concave-up, and there is no Pareto optimum. At high d_{targ} (bottom row of **Figure 5—figure supplement 2**), the searcher either barely reaches, and does so at $\theta_{\text{contact}} = 0$, therefore providing high directional information, or D_θ is high, and the searcher fails to reach, and therefore also fails to provide directional information. So, there is no trade-off. At intermediate d_{targ}, the curve transitions from concave-up bull's horn to the no-trade-off diagonal line. Interestingly, it does so by bending forward, forming a loop, and closing the loop as the low-D_θ tip moves toward the origin. At these intermediate d_{targ} values, the loop offers a concave-down region with a Pareto optimum.

Discussion

As long-range cellular projections like airinemes continue to be discovered in multicellular systems, their mathematical characterization will become increasingly valuable, mirroring the mathematical characterization of diffusion-mediated cell–cell signals. We have measured the in situ shape of airinemes, and find agreeable fit to a finite, unobstructed PRW model, rather than Levy or diffusion-like motion. The mean square curvature, or equivalently the directional persistent length, is close to that which allows optimal search efficiency for target cells. Since airineme tip motion is driven by macrophages, our results have implications for macrophage cell motility, which is relevant in other macrophage-dependent processes like wound healing and infection (**Sun et al., 2019**; **Achouri et al., 2015**).

The growing catalog of non-canonical cellular protrusions (**Eom, 2020**; **Yamashita et al., 2018**; **Caviglia and Ober, 2018**; **Sanders et al., 2013**; **Bressloff and Kim, 2019**; **Inaba et al., 2015**; **Kornberg and Roy, 2014**; **Parker et al., 2017**; **Subramanian et al., 2018**; **Wang and Gerdes, 2015**) includes strikingly different shapes. For example, some tunneling nanotubes in cancer cells (**Parker et al., 2017**) are straight compared to airinemes. They also have different functions. For example, nanotubes in PC12 cells serve as conduits for organelles (**Wang and Gerdes, 2015**). This raises an intriguing possibility that different protrusions have a shape optimized for different functions. Besides search success probability and directional information, one obvious candidate for optimization is the efficient transport of signaling molecules after contact has been established (**Bressloff and Kim, 2018**; **Kim and Bressloff, 2018**). This might prefer shorter protrusion length, and therefore favor straight morphologies. In the future, it would be intriguing to compare all known non-canonical protrusions in light of the three performance objectives, and others.

Since the airineme tip's motion is linked to macrophage motion, these results also inform cell migration patterns. Variants of the PRW model have been found to describe cell migration (**Harrison and Baker, 2018**; **Weavers et al., 2016**). Specifically, a related model was found to accurately describe macrophages in zebrafish (**Jones et al., 2015**). Two observations from **Jones et al., 2015** are particularly relevant to our work: that macrophages in zebrafish demonstrate a mix of directional persistence

and randomness, and that their migration patterns adapt to circumstance (specifically, in their case, distance to wound and time since wounding).

Mathematically, the finite PRW process is equivalent to the worm-like chain model, for which exact formula have been derived for the tip location (*Spakowitz and Wang, 2005*; *Mehraeen et al., 2008*). The contact probability corresponds to a survival probability in the presence of an absorbing disk representing the target cell, and therefore an integral of the formulae in *Spakowitz and Wang, 2005*; *Mehraeen et al., 2008*. There is an opportunity to find analytic (asymptotic or exact) expressions for the contact probabilities, which would obviate the need for stochastic simulation.

The cell–cell interactions mediated by airinemes contribute to large-scale pattern formation in zebrafish, a subject of previous mathematical modeling (*Volkening and Sandstede, 2015*; *Volkening and Sandstede, 2018*; *Nakamasu et al., 2009*). Our results provide a contact probability per airineme, setting an upper bound on the ability of cells to communicate via this modality, which is itself a function of cell density (related to d_{targ} in our notation). Thus, our results may inform future pattern formation models. In the reciprocal direction, these models may provide information about the distribution of target cells, which may significantly affect search efficiencies.

Materials and methods

Key resources table

Reagent type (species) or resource	Designation	Source or reference	Identifiers	Additional information
Genetic reagent (*Danio rerio*)	Tg(tyrp1b: PALM-mCherry)	*Eom et al., 2015*	RRID:ZDB-TGCONSTRCT-141218-3	
Recombinant DNA reagent	aox5: palmEGFP (plasmid)	*Eom et al., 2015*	RRID:ZDB-TGCONSTRCT-160414-1	
Software	ImageJ	http://imagej.nih.gov/ij/	RRID:SCR_003070	
Software	MATLAB R2021b	http://www.mathworks.com/		

Zebrafish husbandry and maintenance

Adult zebrafish were maintained at 28.5°C on a 16 hr:8 hr light:dark cycle. Fish stocks of *Tg(tyrp-1b:palmmCherry)*[wp.rt11] (*McMenamin et al., 2014*) were used. Embryos were collected in E3 medium (5.0 mM NaCl, 0.17 mM KCl, 0.33 mM CaCl₂, 0.33 mM MgCl₂·6H₂O, adjusted to pH 7.2–7.4) in Petri dishes by in vitro fertilization as described in Westerfield with modifications (*Westerfield, 2004*). Unfertilized and dead embryos were removed 5 hr post-fertilization (hpf) and 1-day post-fertilization (dpf). Fertilized embryos were kept in E3 medium at 28.5°C until 5 dpf, at which time they were introduced to the main system until they were ready for downstream procedures. All animal work in this study was conducted with the approval of the University of California Irvine Institutional Animal Care and Use Committee (protocol #AUP-19-043) in accordance with institutional and federal guidelines for the ethical use of animals.

Time-lapse and static imaging

The transgenic embryos, *Tg(tyrp1b:palmmCherry)*, were injected with the construct drive membrane-bound EGFP under the aox5 promoter to visualize airinemes in xanthophore lineages and melanophores (*Eom et al., 2015*). Zebrafish larvae of 7.5 SSL were staged following *Parichy et al., 2009* prior to explant preparation for ex vivo imaging of pigment cells in their native tissue environment as described by *Budi et al., 2011* and *Eom et al., 2012*. Time-lapse images, acquired at 5 min intervals for 12 hr, and static images were taken at ×40 (water-emulsion objective) on a Leica SP8 confocal microscope with resonant scanner.

Model definitions, simulation, and analysis

In the finite-length PRW model, the position of the airineme tip at time t is given by

$$\frac{dx}{dt} = v \cos(\theta(t))$$

(2)

$$\frac{dy}{dt} = v \sin\left(\theta(t)\right) \tag{3}$$

$$d\theta = \sqrt{2D_\theta}\, dW_t \tag{4}$$

where W_t is a Wiener process, and D_θ is related to the directional persistence length l_p in 2D by $D_\theta = v/2l_p$.

The MSD for PRWs is (**Wu et al., 2014**; **Sadjadi et al., 2020**)

$$\langle r^2 \rangle = 4l_p v t \left(1 - \frac{2l_p}{vt}\left(1 - \exp\left(-\frac{vt}{2l_p}\right)\right)\right). \tag{5}$$

To simulate this model, we use an Euler–Maruyama scheme with timestep $\Delta t \ll 1/D_\theta$, implemented in MATLAB (The MathWorks). To validate these simulations, at two limits of D_θ, search contact probabilities can be solved analytically (**Figure 3A and B**, filled circles). First, the straight limit $D_\theta \rightarrow 0$. Suppose an airineme searches for the target cell centered at $(0,0)$ with radius r_{targ}, and the airineme emanates from a source at $(r_{\text{targ}} + d_{\text{targ}}, 0)$. Let ϕ be the angle between the hitting point on the target cell and the center line. Then,

$$\phi = \frac{\pi}{2} - \arccos\left(\frac{r_{\text{targ}}}{r_{\text{targ}} + d_{\text{targ}}}\right) \tag{6}$$

and $P_{\text{contact}} = \phi/\pi$. At the other limit, $l_P \ll d_{\text{targ}}$, the PRW is approximately equivalent to diffusion with coefficient $D = v^2/2D_\theta$. For a finite time $0 < t < l_{\text{max}}/v$ diffusive search process, the probability of hitting the target cell is $P_{\text{contact}} = 1 - S(r, t)$, where $S(r, t)$ denotes the survival probability, which evolves according to

$$\partial S/\partial t = D\nabla^2 S \tag{7}$$

with $S(r, t) = 0$ on the surface of the target cell. We solve this PDE and display results in **Figure 3A and B**, blue circles. For these validations, the D_θ values were chosen to fit the blue circles onto the plot.

Image analysis and model fitting

In order to estimate uncertainty in our analysis method, we used model convolution (**Figure 4—figure supplement 1**, **Gardner et al., 2010**). Specifically, we first measured the experimental signal-to-noise ratio and point spread function. We then simulated airinemes with a ground-truth curvature value and convoluted the simulated images with a Gaussian kernel with the signal-to-noise ratio and point spread function measured from experimental data. Since there is a manual step in this analysis pipeline, independent analyses by five people were performed on both simulated data and experimental data. For simulated data, the difference between simulated and estimated D_θ was less than 7% in all cases and usually $\sim 2\%$.

The extracted data and analysis routines are available openly at: https://github.com/sohyeon-parkgithub/Airineme-optimal-target-search, (copy archived at swh:1:rev:366ad6e1e3e5061c0cf-395c8e3be784872903922; **Park, 2021**).

Directional information

To measure the directional information that, stochastically, an airineme provides its target cell, we use the Fisher information,

$$I_1(\theta_{\text{origin}}) = \mathbb{E}\left(-\frac{\partial^2}{\partial\theta_{\text{origin}}^2}\log p\left(\theta_{\text{target}}|\theta_{\text{origin}}\right)\right). \tag{8}$$

This quantity can be intuitively understood by noting that, for Gaussian distributions, Fisher information is the inverse of the variance. So, high variance implies low information and low variance implies high information. If multiple independent and identically distributed airinemes provide information to the target cell, then the probability densities of each airineme multiply, and the Fisher information is $I(\theta_{\text{origin}}) = n_{hit} \cdot I_1(\theta_{\text{origin}})$, where n_{hit} is the number of successful attempts, which is proportional to P_{contact}. Therefore, we define the modified Fisher information as

$$\text{Modifed FI} = I(\text{origin}) \cdot P_{\text{contact}}. \tag{9}$$

With this modification, a target cell that receives almost no airinemes will score low in directional information.

Experimental measurement of directional information

Images capturing incidences of airinemes with membrane-bound vesicles extended from xanthoblasts, stabilizing on melanophores were captured and imported into ImageJ for angle analysis between (1) originating point of airinemes on xanthoblasts, (2) center of target cells (i.e., melanophores), and (3) docking site of airineme vesicles on target cells. Two intersecting lines were drawn as follows: (1) connect the originating point of an airineme on a xanthoblast with the center of the target melanophore to draw the first line, and (2) connect the center of the target melanophore to the docking site of the airineme vesicle on the target melanophore to draw the second line. The angle between the three points connected by the two intersecting lines was then generated automatically with the angle tool in ImageJ. Coordinates of each point and the corresponding angle were recorded with ImageJ and exported to an Excel worksheet for further analysis. Each angle was assigned a ± sign in the 180° system based on the relative location of the three points at the time of the airineme incident. The 0° line was defined as the line passing through the center of the target melanophore. Thus, a positive angle was assigned when the originating point of an airineme on a xanthoblast lies on the 0° line with the docking site of airineme vesicles on the target melanophore lies above the 0° line, and vice versa.

The extracted data and analysis routines are available openly at https://github.com/sohyeonparkgithub/Airineme-optimal-target-search.

Acknowledgements

Additional information

Author contributions

Sohyeon Park, Data curation, Formal analysis, Investigation, Software, Validation, Visualization, Writing – original draft, Writing – review and editing; Hyunjoong Kim, Conceptualization, Investigation, Mathematical model development, Software, Validation; Yi Wang, Formal analysis, Investigation; Dae Seok Eom, Conceptualization, Funding acquisition, Methodology, Project administration, Supervision, Writing – original draft, Writing – review and editing; Jun Allard, Conceptualization, Funding acquisition, Project administration, Supervision, Writing – original draft, Writing – review and editing

Author ORCIDs
Hyunjoong Kim http://orcid.org/0000-0002-3534-2102
Yi Wang http://orcid.org/0000-0001-7409-4335
Dae Seok Eom http://orcid.org/0000-0002-0617-8788
Jun Allard http://orcid.org/0000-0002-2758-4515

Ethics
All animal work in this study was conducted with the approval of the University of California Irvine Institutional Animal Care and Use Committee (Protocol #AUP-19-043) in accordance with institutional and federal guidelines for the ethical use of animals.

Decision letter and Author response
Decision letter https://doi.org/10.7554/eLife.75690.sa1
Author response https://doi.org/10.7554/eLife.75690.sa2

Additional files

Supplementary files
• Transparent reporting form

Data availability
Data and computational scripts are available in a repository mentioned in the manuscript (on GitHub) https://github.com/sohyeonparkgithub/Airineme-optimal-target-search, (copy archived at swh:1:rev:366ad6e1e3e5061c0cf395c8e3be784872903922).

The following dataset was generated:

Author(s)	Year	Dataset title	Dataset URL	Database and Identifier
Park S, Kim H, Li Y, Eom DS, Allard J	2021	Airineme experimental data and codes	https://github.com/sohyeonparkgithub/Airineme-optimal-target-search	GitHub, GitHub

References
Achouri S, Wright JA, Evans L, Macleod C, Fraser G, Cicuta P, Bryant CE. 2015. The frequency and duration of Salmonella-macrophage adhesion events determines infection efficiency. *Philosophical Transactions of the Royal Society of London. Series B, Biological Sciences* 370:20140033. DOI: https://doi.org/10.1098/rstb.2014.0033, PMID: 25533091

Alon U. 2009. How to choose a good scientific problem. *Molecular Cell* 35:726–728. DOI: https://doi.org/10.1016/j.molcel.2009.09.013, PMID: 19782018

Barton JP, Sontag ED. 2013. The energy costs of insulators in biochemical networks. *Biophysical Journal* 104:1380–1390. DOI: https://doi.org/10.1016/j.bpj.2013.01.056, PMID: 23528097

Berg HC, Purcell EM. 1977. Physics of chemoreception. *Biophysical Journal* 20:193–219. DOI: https://doi.org/10.1016/S0006-3495(77)85544-6, PMID: 911982

Berg HC. 1993. Random Walks in Biology. New Jersey, United States: Princeton University Press.

Bialek W, Setayeshgar S. 2008. Cooperativity, sensitivity, and noise in biochemical signaling. *Physical Review Letters* 100:258101. DOI: https://doi.org/10.1103/PhysRevLett.100.258101, PMID: 18643705

Bressloff PC, Kim H. 2018. Bidirectional transport model of morphogen gradient formation via cytonemes. *Physical Biology* 15:026010. DOI: https://doi.org/10.1088/1478-3975/aaa64c, PMID: 29313834

Bressloff PC, Kim H. 2019. Search-and-capture model of cytoneme-mediated morphogen gradient formation. *Physical Review. E* 99:052401. DOI: https://doi.org/10.1103/PhysRevE.99.052401, PMID: 31212424

Bressloff PC. 2020. Directed intermittent search with stochastic resetting. *Journal of Physics A* 53:105001. DOI: https://doi.org/10.1088/1751-8121/ab7138

Budi EH, Patterson LB, Parichy DM. 2011. Post-embryonic nerve-associated precursors to adult pigment cells: genetic requirements and dynamics of morphogenesis and differentiation. *PLOS Genetics* 7:e1002044. DOI: https://doi.org/10.1371/journal.pgen.1002044, PMID: 21625562

Caviglia S, Ober EA. 2018. Non-conventional protrusions: the diversity of cell interactions at short and long distance. *Current Opinion in Cell Biology* 54:106–113. DOI: https://doi.org/10.1016/j.ceb.2018.05.013, PMID: 29890397

De Bruyne B, Randon-Furling J, Redner S. 2020. Optimization in First-Passage Resetting. *Physical Review Letters* 125:050602. DOI: https://doi.org/10.1103/PhysRevLett.125.050602, PMID: 32794864

Endres RG, Wingreen NS. 2009. Maximum likelihood and the single receptor. *Physical Review Letters* **103**:158101. DOI: https://doi.org/10.1103/PhysRevLett.103.158101, PMID: 19905667

Eom DS, Inoue S, Patterson LB, Gordon TN, Slingwine R, Kondo S, Watanabe M, Parichy DM. 2012. Melanophore migration and survival during zebrafish adult pigment stripe development require the immunoglobulin superfamily adhesion molecule Igsf11. *PLOS Genetics* **8**:e1002899. DOI: https://doi.org/10.1371/journal.pgen.1002899, PMID: 22916035

Eom DS, Bain EJ, Patterson LB, Grout ME, Parichy DM. 2015. Long-distance communication by specialized cellular projections during pigment pattern development and evolution. *eLife* **4**:e12401. DOI: https://doi.org/10.7554/eLife.12401, PMID: 26701906

Eom DS, Parichy DM. 2017. A macrophage relay for long-distance signaling during postembryonic tissue remodeling. *Science (New York, N.Y.)* **355**:1317–1320. DOI: https://doi.org/10.1126/science.aal2745, PMID: 28209639

Eom DS. 2020. Airinemes: thin cellular protrusions mediate long-distance signalling guided by macrophages. *Open Biology* **10**:200039. DOI: https://doi.org/10.1098/rsob.200039, PMID: 32810422

Fisher RA. 1997. On the mathematical foundations of theoretical statistics. *Philosophical Transactions of the Royal Society of London. Series A, Containing Papers of A Mathematical or Physical Character* **222**:309–368. DOI: https://doi.org/10.1098/rsta.1922.0009

Fricke GM, Letendre KA, Moses ME, Cannon JL. 2016. Persistence and Adaptation in Immunity: T Cells Balance the Extent and Thoroughness of Search. *PLOS Computational Biology* **12**:e1004818. DOI: https://doi.org/10.1371/journal.pcbi.1004818, PMID: 26990103

Gardner MK, Sprague BL, Pearson CG, Cosgrove BD, Bicek AD, Bloom K, Salmon ED, Odde DJ. 2010. Model Convolution: A Computational Approach to Digital Image Interpretation. *Cellular and Molecular Bioengineering* **3**:163–170. DOI: https://doi.org/10.1007/s12195-010-0101-7, PMID: 20461132

Govern CC, ten Wolde PR. 2012. Fundamental limits on sensing chemical concentrations with linear biochemical networks. *Physical Review Letters* **109**:218103. DOI: https://doi.org/10.1103/PhysRevLett.109.218103, PMID: 23215617

Großmann R, Peruani F, Bär M. 2016. Diffusion properties of active particles with directional reversal. *New Journal of Physics* **18**:043009. DOI: https://doi.org/10.1088/1367-2630/18/4/043009

Harrison JU, Baker RE. 2018. The impact of temporal sampling resolution on parameter inference for biological transport models. *PLOS Computational Biology* **14**:e1006235. DOI: https://doi.org/10.1371/journal.pcbi.1006235, PMID: 29939995

Hassan AR, Biel T, Umulis DM, Kim T. 2019. Interplay Between the Persistent Random Walk and the Contact Inhibition of Locomotion Leads to Collective Cell Behaviors. *Bulletin of Mathematical Biology* **81**:3301–3321. DOI: https://doi.org/10.1007/s11538-019-00585-1, PMID: 30788690

Holy TE, Leibler S, Silkworth WT, Nardi IK, Cimini D, Mogilner A. 1994. Dynamic instability of microtubules as an efficient way to search in space. *PNAS* **91**:5682–5685. DOI: https://doi.org/10.1073/pnas.91.12.5682, PMID: 8202548

Hu B, Chen W, Rappel WJ, Levine H. 2010. Physical limits on cellular sensing of spatial gradients. *Physical Review Letters* **105**:048104. DOI: https://doi.org/10.1103/PhysRevLett.105.048104, PMID: 20867888

Inaba M, Buszczak M, Yamashita YM. 2015. Nanotubes mediate niche-stem-cell signalling in the *Drosophila* testis. *Nature* **523**:329–332. DOI: https://doi.org/10.1038/nature14602, PMID: 26131929

Jones PJM, Sim A, Taylor HB, Bugeon L, Dallman MJ, Pereira B, Stumpf MPH, Liepe J. 2015. Inference of random walk models to describe leukocyte migration. *Physical Biology* **12**:066001. DOI: https://doi.org/10.1088/1478-3975/12/6/066001, PMID: 26403334

Khatami M, Wolff K, Pohl O, Ejtehadi MR, Stark H. 2016. Active Brownian particles and run-and-tumble particles separate inside a maze. *Scientific Reports* **6**:1–10. DOI: https://doi.org/10.1038/srep37670, PMID: 27876867

Kim H, Bressloff PC. 2018. Direct vs. Synaptic Coupling in a Mathematical Model of Cytoneme-Based Morphogen Gradient Formation. *SIAM Journal on Applied Mathematics* **78**:2323–2347. DOI: https://doi.org/10.1137/18M1179699

Kornberg TB, Roy S. 2014. Cytonemes as specialized signaling filopodia. *Development (Cambridge, England)* **141**:729–736. DOI: https://doi.org/10.1242/dev.086223, PMID: 24496611

Lawley SD, Lindsay AE, Miles CE. 2020. Receptor Organization Determines the Limits of Single-Cell Source Location Detection. *Physical Review Letters* **125**:018102. DOI: https://doi.org/10.1103/PhysRevLett.125.018102, PMID: 32678664

Lawley SD, Madrid JB. 2020. A Probabilistic Approach to Extreme Statistics of Brownian Escape Times in Dimensions 1, 2, and 3. *Journal of Nonlinear Science* **30**:1207–1227. DOI: https://doi.org/10.1007/s00332-019-09605-9

McMenamin SK, Bain EJ, McCann AE, Patterson LB, Eom DS, Waller ZP, Hamill JC, Kuhlman JA, Eisen JS, Parichy DM. 2014. Thyroid hormone-dependent adult pigment cell lineage and pattern in zebrafish. *Science (New York, N.Y.)* **345**:1358–1361. DOI: https://doi.org/10.1126/science.1256251, PMID: 25170046

Mehraen S, Sudhanshu B, Koslover EF, Spakowitz AJ. 2008. End-to-end distribution for a wormlike chain in arbitrary dimensions. *Physical Review. E, Statistical, Nonlinear, and Soft Matter Physics* **77**:061803. DOI: https://doi.org/10.1103/PhysRevE.77.061803, PMID: 18643291

Mogre SS, Christensen JR, Niman CS, Reck-Peterson SL, Koslover EF. 2020. Hitching a Ride: Mechanics of Transport Initiation through Linker-Mediated Hitchhiking. *Biophysical Journal* **118**:1357–1369. DOI: https://doi.org/10.1016/j.bpj.2020.01.024, PMID: 32061275

Nakamasu A, Takahashi G, Kanbe A, Kondo S. 2009. Interactions between zebrafish pigment cells. *PNAS* **106**:8429–8434. DOI: https://doi.org/10.1073/pnas.0808622106

Parichy DM, Elizondo MR, Mills MG, Gordon TN, Engeszer RE. 2009. Normal table of postembryonic zebrafish development: staging by externally visible anatomy of the living fish. *Developmental Dynamics* **238**:2975–3015. DOI: https://doi.org/10.1002/dvdy.22113, PMID: 19891001

Park S. 2021. Airineme-optimal-target-search. swh:1:rev:366ad6e1e3e5061c0cf395c8e3be784872903922. GitHub. https://github.com/sohyeonparkgithub/Airineme-optimal-target-search

Parker I, Evans KT, Ellefsen K, Lawson DA, Smith IF. 2017. Lattice light sheet imaging of membrane nanotubes between human breast cancer cells in culture and in brain metastases. *Scientific Reports* **7**:1–7. DOI: https://doi.org/10.1038/s41598-017-11223-y, PMID: 28887508

Paul R, Wollman R, Silkworth WT, Nardi IK, Cimini D, Mogilner A. 2009. Computer simulations predict that chromosome movements and rotations accelerate mitotic spindle assembly without compromising accuracy. *PNAS* **106**:15708–15713. DOI: https://doi.org/10.1073/pnas.0908261106, PMID: 19717443

Ryu HJ, Lee JM, Jang HW, Park HC, Rhyu IJ, Kim IH. 2016. Morphologic Changes of Zebrafish Melanophore after Intense Pulsed Light and Q-Switched Nd:YAG Laser Irradiation. *Annals of Dermatology* **28**:711–717. DOI: https://doi.org/10.5021/ad.2016.28.6.711, PMID: 27904270

Sadjadi Z, Zhao R, Hoth M, Qu B, Rieger H. 2020. Migration of Cytotoxic T Lymphocytes in 3D Collagen Matrices. *Biophysical Journal* **119**:2141–2152. DOI: https://doi.org/10.1016/j.bpj.2020.10.020, PMID: 33264597

Sanders TA, Llagostera E, Barna M. 2013. Specialized filopodia direct long-range transport of SHH during vertebrate tissue patterning. *Nature* **497**:628–632. DOI: https://doi.org/10.1038/nature12157, PMID: 23624372

Schakenraad K, Ravazzano L, Sarkar N, Wondergem JAJ, Merks RMH, Giomi L. 2020. Topotaxis of active Brownian particles. *Physical Review. E* **101**:032602. DOI: https://doi.org/10.1103/PhysRevE.101.032602, PMID: 32289917

Schuss Z, Basnayake K, Holcman D. 2019. Redundancy principle and the role of extreme statistics in molecular and cellular biology. *Physics of Life Reviews* **28**:52–79. DOI: https://doi.org/10.1016/j.plrev.2019.01.001, PMID: 30691960

Spakowitz AJ, Wang ZG. 2005. End-to-end distance vector distribution with fixed end orientations for the wormlike chain model. *Physical Review E* **72**:041802. DOI: https://doi.org/10.1103/PhysRevE.72.041802

Subramanian A, Kanzaki LF, Galloway JL, Schilling TF. 2018. Mechanical force regulates tendon extracellular matrix organization and tenocyte morphogenesis through TGFbeta signaling. *eLife* **7**:e38069. DOI: https://doi.org/10.7554/eLife.38069

Sun Y, Reid B, Ferreira F, Luxardi G, Ma L, Lokken KL, Zhu K, Xu G, Sun Y, Ryzhuk V, Guo BP, Lebrilla CB, Maverakis E, Mogilner A, Zhao M, Schneider DS. 2019. Infection-generated electric field in gut epithelium drives bidirectional migration of macrophages. *PLOS Biology* **17**:e3000044. DOI: https://doi.org/10.1371/journal.pbio.3000044

Tejedor V, Voituriez R, Bénichou O. 2012. Optimizing persistent random searches. *Physical Review Letters* **108**:088103. DOI: https://doi.org/10.1103/PhysRevLett.108.088103, PMID: 22463578

Viswanathan G, da Luz MGE, Raposo EP, Stanley HE. 2011. The Physics of Foraging. Cambridge: Cambridge University Press. DOI: https://doi.org/10.1017/CBO9780511902680

Volkening A, Sandstede B. 2015. Modelling stripe formation in zebrafish: an agent-based approach. *Journal of the Royal Society, Interface* **12**:112. DOI: https://doi.org/10.1098/rsif.2015.0812, PMID: 26538560

Volkening A, Sandstede B. 2018. Iridophores as a source of robustness in zebrafish stripes and variability in Danio patterns. *Nature Communications* **9**:1–14. DOI: https://doi.org/10.1038/s41467-018-05629-z, PMID: 30104716

Volkening A. 2020. Linking genotype, cell behavior, and phenotype: multidisciplinary perspectives with a basis in zebrafish patterns. *Current Opinion in Genetics & Development* **63**:78–85. DOI: https://doi.org/10.1016/j.gde.2020.05.010, PMID: 32604031

Wang X, Gerdes HH. 2015. Transfer of mitochondria via tunneling nanotubes rescues apoptotic PC12 cells. *Cell Death and Differentiation* **22**:1181–1191. DOI: https://doi.org/10.1038/cdd.2014.211, PMID: 25571977

Weavers H, Liepe J, Sim A, Wood W, Martin P, Stumpf MPH. 2016. Systems Analysis of the Dynamic Inflammatory Response to Tissue Damage Reveals Spatiotemporal Properties of the Wound Attractant Gradient. *Current Biology* **26**:1975–1989. DOI: https://doi.org/10.1016/j.cub.2016.06.012, PMID: 27426513

Westerfield M. 2004. A Guide for the Laboratory Use of Zebrafish. Eugene, OR: University of Oregon Press.

Wu PH, Giri A, Sun SX, Wirtz D. 2014. Three-dimensional cell migration does not follow a random walk. *PNAS* **111**:3949–3954. DOI: https://doi.org/10.1073/pnas.1318967111, PMID: 24594603

Yamashita YM, Inaba M, Buszczak M. 2018. Specialized Intercellular Communications via Cytonemes and Nanotubes. *Annual Review of Cell and Developmental Biology* **34**:59–84. DOI: https://doi.org/10.1146/annurev-cellbio-100617-062932, PMID: 30074816

Zurzolo C. 2021. Tunneling nanotubes: Reshaping connectivity. *Current Opinion in Cell Biology* **71**:139–147. DOI: https://doi.org/10.1016/j.ceb.2021.03.003, PMID: 33866130